Lab on a Chip

Development of a Simultaneous Electrorotation Device with Microwells for Monitoring the Rotation Rates of Multiple Single Cells upon Chemical Stimulation

Journal:	*Lab on a Chip*
Manuscript ID	LC-ART-07-2022-000627.R1
Article Type:	Paper
Date Submitted by the Author:	31-Oct-2022
Complete List of Authors:	Suzuki, Masato; University of Hyogo - Harima Science and Technology Campus, Graduate School of Science Kawai, Shikiho; University of Hyogo - Harima Science and Technology Campus, Graduate School of Science Fei, Shee; Kyushu University, Department of Advanced Information Technology Yamada, Ryoga; University of Hyogo - Harima Science and Technology Campus, Graduate School of Science Uchida, Seiichi; Kyushu University, Department of Advanced Information Technology Yasukawa, Tomoyuki; University of Hyogo - Harima Science and Technology Campus, Graduate School of Science

ARTICLE

Development of a Simultaneous Electrorotation Device with Microwells for Monitoring the Rotation Rates of Multiple Single Cells upon Chemical Stimulation

Received 00th January 20xx,
Accepted 00th January 20xx

DOI: 10.1039/x0xx00000x

Masato Suzuki,[a,b,*] Shikiho Kawai,[a] Chean Fei Shee,[c] Ryoga Yamada[a], Seiichi Uchida[c] and Tomoyuki Yasukawa[a,b,*]

Here, we described a unique simultaneous electrorotation (ROT) device for monitoring the rotation rate of Jurkat cells via chemical stimulation without fluorescent labeling and an algorithm for estimating cell rotation rates. The device comprised two pairs of interdigitated array electrodes that were stacked orthogonally through a 20-μm-thick insulating layer with rectangular microwells. Four microelectrodes (two were patterned on the bottom of the microwells and the other two on the insulating layer) were arranged on each side of the rectangular microwells. The cells, which were trapped in the microwells, underwent ROT when AC voltages were applied to the four microelectrodes to generate a rotating electric field. These microwells maintained the cells even in fluid flows. Thereafter, the ROT rates of the trapped cells were estimated and monitored during the stimulation. We demonstrated the feasibility of estimating the chemical efficiency of cells by monitoring the ROT rates of the cells. After introducing a Jurkat cell suspension into the device, the cells were subjected to ROT by applying an AC signal. Further, the rotating cells were chemically stimulated by adding an ionomycin (a calcium ionophore)-containing aliquot. The ROT rate of the ionomycin-stimulated cells decreased gradually to 90% of the initial rate after 30 s. The ROT rate was reduced by an increase in membrane capacitance. Thus, our device enabled the simultaneous chemical stimulation-induced monitoring of the alterations in the membrane capacitances of many cells without fluorescent labeling.

Introduction

Cell rotations are important cell-manipulation methods for determining cell morphology accurately and for performing cell surgery precisely, including selective extraction of targeted organelles and injection of foreign genes into the nucleus.[1] Various unique methods for cell rotation have been proposed. Optical tweezers have been widely used in cell surgery to position cells precisely for the insertion of glass capillaries.[2–4] Magnetic fields have also been used to rotate cells modified with magnetic particles.[5–7] Rotational motion of cells is induced by convective hydrodynamic forces generated by acoustic waves in microfluidic channels.[8,9] This method has been applied to obtain accurate morphology not only of cells,[10–12] but also of the entire zebrafish body.[13] It is also possible to analyze the cell type and state in a label-free manner by measuring the rotation rate of the cell. This single-cell analysis method based on the rotation of individual cells was achieved by an electro-rotation (ROT) induced by a rotational electric field.[14]

ROT is a phenomenon in which cells rotate continuously in a rotational electric field owing to torques that are induced by the electrostatic interactions between the field and polarization charges in the cells.[15] Since ROT rates mainly depend on the membrane capacitance and cytoplasm conductivity of single cells, they have been employed for the noninvasive and accurate characterization of the electrical properties of such cells. For example, monocytes and T cells have been distinguished via the measurements of their ROT rates based on the differences in their membrane capacitances;[16] membrane capacitances reflect the roughness of cell membrane surfaces. Via scanning electron microscopy, several microvilli (length = 50–200 nm) were observed on the surface of T cells with high membrane capacitances, while none was observed on the surface of monocytes with low membrane capacitances. In this way, the measurement of ROT can distinguish the ultrastructure of the surface of the cell

[a] Graduate School of Science, University of Hyogo, Hyogo, Japan.
[b] Advanced Medical Engineering Research Institute, University of Hyogo, Hyogo, Japan
[c] Department of Advanced Information Technology, Kyushu University, Fukuoka, Japan.
[d] Corresponding Authors
Prof. Tomoyuki Yasukawa,
Graduate School of Science, University of Hyogo, 3-2-1, Kouto, Kamigori, Ako, Hyogo, 678-1297, Japan.
E-mail: yasu@sci.u-hyogo.ac.jp

Prof. Masato Suzuki,
E-mail: suzuki@sci.u-hyogo.ac.jp

Electronic Supplementary Information (ESI) available: [details of any supplementary information available should be included here]. See DOI: 10.1039/x0xx00000x

membrane via the differences in the rotation rate. Further, ROT has been employed to identify the cell cycle,[17] detect the activation of osmotic-sensitive channels,[18,19] detect human neutrophil activation by the chemotactic factor,[20] distinguish the differentiation state for erythroleukemia cells,[21,22] distinguish cancer cells exhibiting drug resistivity via the overexpression of glycoproteins,[23] obtain the precise 3D cell image,[24,25] and determine three biophysical parameters (shear modulus, steady-state viscosity, and relaxation time from the stretching deformation) by combination with the optical stretching method.[26]

ROT has been traditionally performed with four planer square electrodes that were arranged symmetrically around a point. The cells, which were collected at the center of the four electrodes, were rotated continuously via the application of sine waves (with $\pi/2$ differences in each phase) in the frequency range of the negative dielectrophoresis (n-DEP). The ROT-inducing electrodes were produced via a traditional photolithographic microfabrication method. However, only a few cells that were trapped at the center of the electrodes, were targeted for ROT measurement. Unfortunately, the ROT behavior was disturbed by a fluidic flow through which other cells arrived at the target cells that were trapped at the center. Furthermore, the friction and adhesion between the rotating cells and electrode substrate interfered with the rotation of the cells. Therefore, the levitation of cells by the laser tweezers,[16,27] and the negative dielectrophoresis[28] during ROT as well as the layout of the octupole electrode comprising upper and lower substrates with four microelectrodes,[29,30] respectively, were proposed to prevent the cells from contacting the substrates. The utilization of cell-levitation techniques facilitated the measurement of the ROT rates within a wide frequency range (from a few kHz to dozens of MHz); however, the number of adaptable cells to ROT measurement via a single operation was limited to a single or few cells. In addition, the optimal placement of electrode was recently calculated by simulations to induce stable ROT over a wide frequency range.[31]

ROT of multiple cells in a single operation (simultaneous ROT) was recently reported.[32–35] We also developed a novel simultaneous ROT device in which two substrates with interdigitated array (IDA) electrodes were orthogonally superimposed via space for introducing cells.[36,37] Although the device facilitated the measurement of the ROT rates of >500 cells via a single operation, the addition of a solution to chemically stimulate the cells disturbed the position of cells during the ROT measurement owing to the levitation of the cells between the two substrates bearing the IDA electrodes. Therefore, we earnestly desired to monitor the ROT rates of many cells without inducing any disturbance during the chemical stimulation.

In this study, we developed a novel microwell array device comprising four microelectrodes to simultaneously investigate the ROT behaviors of multiple cells, following the addition of a chemical stimulant. Two of the electrodes were arranged at the bottom of the microwells on either side, while the other two were placed on either side of the top surface of the microwells. The rotating electric fields were generated by applying AC signals to the four electrodes with $\pi/2$ phase differences, thereby inducing the simultaneous rotations of the cells that were trapped in each microwell. The time-course of the ROT rate was analyzed by adapting a homemade software, which was based on image recognition analysis, to a series of the images of the rotating cells. Although the ROT rate was almost constant when the solution was added to the device, it varied by a few percent. Conversely, the addition of ionomycin as the chemical stimulant gradually reduced the ROT rate probably because of the effect of ionomycin, which increased cytosolic Ca^{2+}, causing the swelling and increase of the plasma membrane and its membrane capacitance, respectively. Our microelectrode device represents a successful platform for detecting cell response to chemical stimulation via ROT instead of fluorescent labeling or the attachment of microelectrodes to the cells.

Materials and Methods

Electrode layout of the ROT device

The layout of the microwell array device is shown in Fig. 1. The device consisted of 225 rectangular microwells (length, 26 μm; width, 20 μm; and height, 20 μm), which equipped two indium tin oxide (ITO) microelectrodes (light gray) at the bottom substrate and two Au microelectrodes (black) at the top plane of the microwells (Fig. 1A). The microwells was designed as a rectangular shape to arrange the four electrodes at approximately the same distance from the center of the microwell. Au layers were employed as the upper electrode to avoid a destruction of the resin layer with microwells with a high-temperature process required to form ITO layer. Fig. S1 shows the schematic of the fabrication process of electrode devices. Further, 16 ITO microband electrodes were patterned on a glass substrate (width, 40 μm; gap, 20 μm; and length, 1 mm) (Fig. S1A). The microwells, which were fabricated by a polyimide-based resin, were patterned with pieces of the ITO microband electrodes at both short sides of the rectangular microwells (Fig. S1B). The height of the microwells was defined by the thickness of the resin. Furthermore, 16 Au microband electrodes (width, 20 μm; gaps, 40 μm; length, 1 mm; and thickness, 100 nm) with rectangular features were patterned

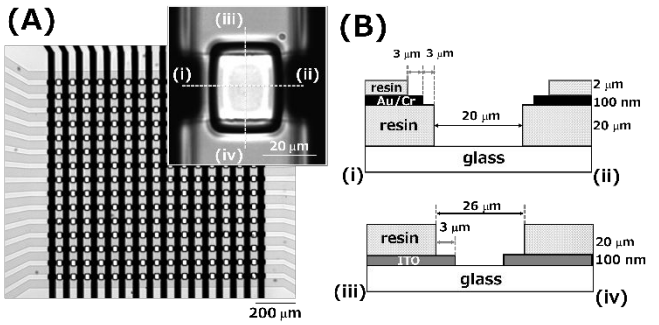

on the polyimide resin orthogonally to the ITO microband electrodes (Fig. S1C). The rectangular features (6 μm × 20 μm)

were placed near the long sides of the microwells with the rectangular shape. The Au microband electrodes were covered with the polyimide-based resin (thickness, 2 μm) except for the rectangular features (3 μm × 20 μm, Fig. S1D). Thus, the microwells were surrounded by four microelectrodes with spatial orthogonal placement; two ITO microelectrodes (3 μm × 20 μm) were patterned on the bottom glass substrate, and two gold microelectrodes (3 μm × 20 μm) were patterned on top of the resin layer beside the long sides of the microwells (Fig. 1A inset and Fig. 1B). The microwell array devices were fabricated by NTT Advanced Technology Corporation (Kawasaki, Japan). A cylindrical poly(dimethylsiloxane) (PDMS) chamber (outer diameter, 15 mm; inner diameter, 10 mm; height, 6 mm; and volume, 470 μL) was placed on the electrode device for pouring the cell suspension for ROT measurement.

Cell preparation for ROT measurement

Human acute lymphocytic leukemia cell lines (Jurkat E6.1) were obtained from the European Collection of Authenticated Cell Cultures. Chronic myelogenous leukemia (K562) was provided by the RIKEN BRC. These cells were cultured in an RPMI 1640 medium (Sigma-Aldrich; St Louis, MO) that was supplemented with 10% fetal bovine serum (Life Technologies; Carlsbad, CA) and 1% penicillin–streptomycin (Wako Pure Chemical Industries; Osaka, Japan) in 5% CO_2 at 37°C. Next, the cultured cells were collected via centrifugation for 5 min at 1000 rpm and resuspended in the ROT solution, which was prepared by mixing an aqueous solution of 300 mM mannitol with the RPMI 1640 medium in a volume ratio of 95:5 and a conductivity of 74 mS m^{-1}. The cell suspension (300 μL) was poured into the PDMS chamber that had been pretreated with the 30 mg mL^{-1} bovine serum albumin-containing ROT solution for 60 min to block the nonspecific adsorption of cells into the device. Afterward, to generate rotating electric fields in all the microwells, an AC voltage with π/2 phase differences was applied to the four electrodes via a function generator (Active Technologies; Ferrara, Italy). An inverted microscope (Nikon Corporation; Tokyo, Japan), which was equipped with a complementary metal–oxide semiconductor camera (The Imaging Source Asia Co., Ltd.; Xizhi District, Taiwan), was employed to observe the rotating cells through a 20× objective lens.

To chemically stimulate the Jurkat cells with ionomycin, a mixture (1 μL) of 90% (v/v) ROT solution and 10% (v/v) dimethyl sulfoxide (DMSO) containing ionomycin with a final concentration of 300 μM was gently added to the top of the cell suspension (300 μL) filled in PDMS chamber after 10 s of inducing ROT. The patterns of cells are different in each experiment. Thus, the cells rotated at the center of the microwells before and after the chemical stimulation were involved to analyze the ROT rates.

Calcium imaging

To monitor the increase in the intracellular calcium concentration during ionomycin stimulation, the Jurkat cells were transfected with CMV-G-GECO1.2 by the Nucleofector™ 2b, following the supplementary manual. CMV-G-GECO1.2 was gifted by Robert Campbell (Addgene plasmid #32446, http://n2t.net/addgene:32446)[38]. Thereafter, the transfected Jurkat cells were cultured for 48 h on cover glasses (diameter, 5 mm) that were pretreated with a 0.01% poly-L-lysin solution (Sigma-Aldrich; St Louis, MO) for 30 min. The glass substrate containing the cells was transferred into the PDMS chamber that had been filled with the Ca^{2+} (2.1 μM)-containing ROT solution. The fluorescence that was generated from the GECO protein was monitored by fluorescence microscopy.

Image recognition analysis for evaluating ROT rates

We obtained sequential grayscale images of the rotating cells with 1920 × 1200 pixels at 30 frames per second (fps) over 60 s to evaluate the rotating rate. The rotation rate was determined by a custom-made software that was based on an image recognition method to describe the following process (the software is available on the GitHub website: https://github.com/jeffshee/cell-rotation/releases/tag/v2.5). First, we manually defined a region of interest (ROI) containing a cell without the microwell and microelectrode edges (Figs. S2A and S2B1). Otsu's thresholding was applied to the cell images in the ROI to distinguish the cell regions from the background.[39] The contour of the cell was extracted employing the OpenCV function findContours to define an inner region of the contour as the cell area (Fig. S2B2); next, the region, except the cell area, was filled with black color. The images with an extracted cell produced movies (see supporting Movie S1). The rotation rates were determined by the consecutive images, as follows: the similarities of the images of the N + Δf frames to an image of the N frame were expressed by a value of −1 to +1 as the normalized cross-correlation (NCC), which was calculated by the normalized correlation function matching method employing the OpenCV function TM_CCOEFF_NORMED. The similarity between the images of frames N and N + Δf was high in proportion to the increase in the NCC value. Thus, $\Delta f_{N,highest}$, which is the number of frames from frame N to the frame with the first maximum NCC value represented the rotation rate. The rotation rate, Ω_N, of the cells at frame N was calculated by the following equation in radian per second.

$$\boldsymbol{\Omega_N = 2\pi \times \frac{30\,fps}{\Delta f_{N,\,highest}}\,radian\,s^{-1}}. \quad \text{(Eq. 1)}$$

Each rotation rate was expressed as a moving average over 30 frames. The rotation rates were also obtained manually from the trajectories of the characteristic points on the surfaces of the rotating cells, as extracted from the movies.

Statistical Analysis

Microsoft Excel software was used for the statistical analysis. Two groups were compared using the Student's t-test if the variances of the two groups were similar by the F-test, otherwise, the Welch's t-

test was used. A significant difference between the two groups was evaluated using a threshold of less than 0.05 for the calculated statistical (p-value and F-value). The date is means× S.E. (standard error).

Results

Theoretical determination of the required frequency for measuring ROT.

We calculated the real and imaginary parts of the Clausius–Mossotti factors, (Re[CM] and Im[CM]), of the Jurkat cell as a function of the frequency to determine the applied frequency for ROT (Fig. S3). The rotation rate and direction of ROT depended on the value of Im[CM]. The theoretical rotation rate, Ω, of ROT is expressed by the following:

$$\boldsymbol{\Omega} = -\frac{\boldsymbol{\varepsilon_o \varepsilon_s}}{\boldsymbol{2\eta}} \boldsymbol{Im[CM]E^2}, \quad \text{(Eq. 2)}$$

where ε_0 and ε_s are the permittivities of the vacuum and ROT solution, respectively; η is the viscosity of the ROT solution; and E is the electric field.[40] A positive value of Im[CM] indicates that the overall value of Ω would be negative and that the direction of the rotation of the cells would be opposite to that of the rotating electric field. To calculate Re[CM] and -Im[CM] in the Jurkat cells, a single-shell model was assumed,[41,42] and the following parameters were utilized: the cell membrane capacitance and cytoplasm conductivity were 9.82 mF m^{-2} and 0.25 S m^{-1}, respectively, following our previous report.[37] The measured average radius of the Jurkat cells was 6.02 μm, and the conductivity and relative permittivity of the extracellular solution (ROT solution) were 74 mS m^{-1} and 78, respectively. The cytoplasm permittivity was set as 103.9 ε_0, following a previous report.[16] The values of Re[CM] and −Im[CM] in the frequency range of 10^4–10^7 Hz are represented in Fig. S3. The cells would be attracted to the edges of the microband electrodes by positive DEP (p-DEP) in the frequency range where Re[CM] is positive. Conversely, they would be repelled from the highest electric field strength regions by n-DEP if Re[CM] was negative. The microwell-trapped cells were attracted to an electrode edge by the p-DEP force that was generated by a slightly unbalanced electric field in the higher-frequency region, while they were occasionally removed from the microwells by the n-DEP force in the lower-frequency region. Therefore, a frequency of 300 kHz, where Re[CM] is close to zero, was employed to rotate the cells. In this frequency, the cells were rotated at approximately maximum owing to the maximum value of Im[CM] with the net DEP force of zero.

Simulation of the electric field distribution in the single-microwell

The three-dimensional distribution of the electric field strength in the microwells was calculated by a finite element method solver (COMSOL Multiphysics, Stockholm, Sweden). AC voltages of sin(ωt) V and sin(ωt+π) V were applied to the two microelectrodes "a" and "c" on the top of the microwell (Fig. S4A), and sin(ωt+π/2) V and sin(ωt+3π/2) V, to microelectrodes "b" and "d" on the bottom of the microwell, respectively. The calculation results of the electric field distributions at t=0, T/8, T/4, 3T/8, and T/2 (where T is the period of the sine wave) were summarized in Fig. S4. The x-y distribution and the direction (red arrows) of the electric field at 15.7 μm above the bottom surface represented the generation of a rotating electric field in the microwell (Fig. S4A). Cross-sectional views of the field strength along line i-ii and line iii-iv in Fig.S4A were shown in Figs S4B and C. It is clearly found that the strong electric field frequently appeared immediately above the bottom surface of the microwell due to electrodes “b” and “d” placed on the bottom surface. Furthermore, the electric field was also formed immediately above the upper end of the microwells between two upper electrodes “a” and “c”, hence the formation of the lower electric field below the upper end of the microwell.

The z-profiles of the field strengths above the center of the microwell were plotted to investigate the position of a relatively low field region (Fig. S5). At t=0 and T/2, the electric field was the highest at the bottom surface and decreased with increasing the distance from the bottom due to no application of voltage to electrodes “a” and “c” placed on the upper surface of microwells. In contrast, the electric field was the lowest at the bottom and increased with increasing the distance at t=T/4. This is due to no application of voltage to electrodes “b” and “d”. In addition, the electric field decreased over 24 μm above the bottom surface due to the contribution of the electric field formed by electrodes "a" and "c" to the upper part in the PDMS chamber. The curve obtained at t=T/8 and 3T/8 plotted between curves obtained at t=0 and t=T/4. It is noted that the relatively low strength was formed at z=15.7 μm and its value was independent of the time. Therefore, cells would levitate to rotate in the microwells in the frequency range for n-DEP. Furthermore, the appearance of the electric field above the upper end of the microwells prevents the removal of cells from microwells by the repulsive force of n-DEP.

Optimization of the duration of cell incubation and concentration of cells for microwells with single-cell occupation

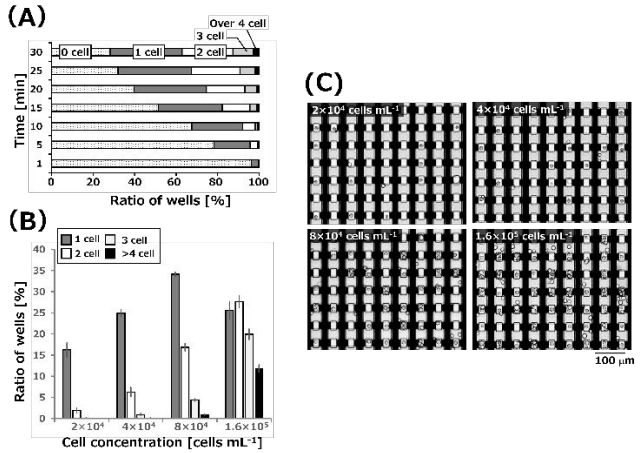

We estimated the number of Jurkat cells in individual microwells when the cell suspension of 300 μL with the concentration 8×10^4 cells mL^{-1} was added to the chamber. The microwells with single-cell occupation increased with the increasing incubation time, while the microwells without cells decreased (Fig. 2A). However, the microwells with multiple occupations also increased. This is due to the random trapping of precipitated cells to microwells with and without cells. The ratio with the single cell occupation reached 35% after 15 min and saturated.

Next, we investigated the occupation ratio with a single cell 15 min after the different concentrations of Jurkat cells were introduced in the chamber (Fig. 2B). The ratio of the microwells with single cells increased with increasing the initial concentrations of cells reaching a maximum (approximately 35%) at the concentration of 8×10^4 cells mL^{-1}. However, the addition of cell suspension with higher concentration leads to the decrease of single-cell occupation because of the increase of the microwells with multiple cells. Furthermore, the increase in the initial concentration led to the increase of the cells on the outside of the microwells (Fig. 2C).

Similar results were obtained from the same experiments using K562 cells (Fig. S6). The ratio with single cell occupation increased with increasing both the incubation time and the initial concentration. However, the ratio reached a maximum (35%) after 10 min that was short compared to that for Jurkat cells. This may be due to the slightly large diameter of K562 cells. Thus, the results suggest that the maximum occupation ratio with single cells was found to be approximately 35% by the sedimentation under the cells' weight in this design of the microwell array. In addition, the duration required to reach the maximum ratio depends on the type of cells.

Evaluation of the rotation rate of the Jurkat cells and K562 cells via image recognition analysis

The Jurkat cell suspension (300 μL), which was adjusted to a concentration of 3.0×10^5 cells mL^{-1}, was poured into the PDMS chamber that was placed on the microwell grid electrode device. After the incubation for 150 s, we gently removed excess cells around the microwells. The cells were captured by their weight in the microwells at the bottom of the device, and the ratio of the wells containing single cells was ~30%. When an AC voltage (300 kHz, 2 Vpp) was applied to the electrode (Fig. 3A(a), (b), (c), and (d)) with a $\pi/2$ phase difference to generate a rotational electric field in the microwells, the cells in the microwells began to rotate in the opposite direction to that of the generated rotating electric field (Movie S2). The cell in the microwell (Fig. 3A(i)) rotated clockwise along its axis at the center of the well (i) via the counterclockwise rotation of the electric field (Fig. 3B and Movie S1). On the other hand, the cell in the microwell (Fig. 3A(ii)) rotated counterclockwise (Fig. S7 and Movie S2). This is because of the formation of the rotational electric field with the opposite directions in neighboring microwells.

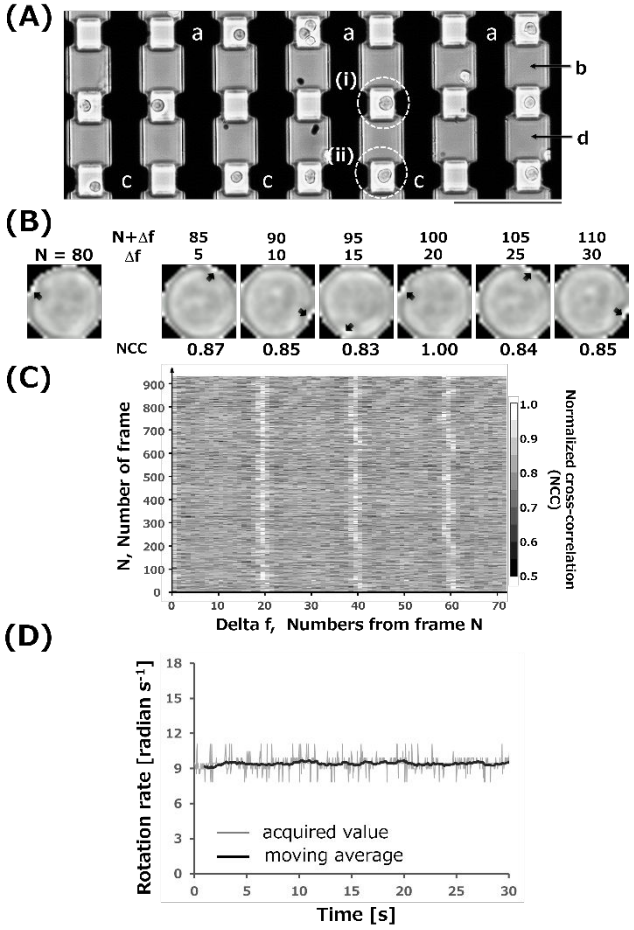

Fig. 3B shows the sequential images from the N = 80 to N = 110 frame of the cell in the microwell (i). The NCC between the images at the N = 80 and 80 + Δf frames was calculated to obtain the number of frames that were required for the single rotation. For this cell, the calculated rotation rate was 9.42 radian s^{-1} because the NCC value of the N = 100 frame image (Δf = 20) was the most similar in 30 frames after the original image of the N = 80 frame. The datasets of the NCC between the images at frames N and N + Δf ($1 \leqq \Delta f \leqq 70$) were obtained by varying the images of frame N from 1 to 900. The values of NCC were visualized by a heatmap. The white region, which corresponded to the frames with high similarity to each original frame (Δf = 0), appeared repeatedly in line patterns at intervals of approximately 20 frames (Fig. 3C). This result

indicates that the cell rotated continuously at a constant rate (0.67 s per single rotation). The representative rotation rates corresponding to each frame were calculated from each $\Delta f_{N,highest}$ that represented the frame number with the highest NCC value in the first cycle of the line pattern. The time-course of the rotation rate is shown in Fig. 3D. The number of rotations was processed employing a moving average over 30 frames to reduce the noise due to the misinterpretation of the cell image induced by the reflection of the edges of the microband electrodes. The rotation rate of this cell was almost constant and 9.42 radian s^{-1} over the whole frame region.

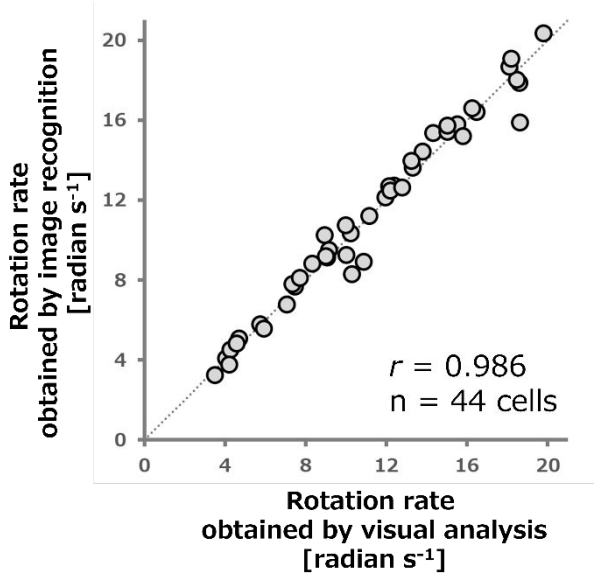

To validate the rotation rates that were obtained via the image recognition method, we manually calculated the rotation rate by tracking the characteristic points on the surface of the same cell in Figure 3. Since the x-axis trajectory of the characteristic point moved periodically between the negative and positive values of the radius (Fig. S8), the rotation rate was calculated by fitting a sine function into this trajectory. The rotation rate obtained by the sine function fitting for 2 s was 9.01 radian s^{-1}, which almost corresponded to that obtained via the image recognition method (9.22 radian s^{-1}, averaged for 2 s). The correlation between the rotation rates that were obtained by both methods was evaluated employing 44 cells that were randomly selected in the microwell array device (Fig. 4). The linear relationship between the rotation rates was observed with the Pearson product–moment correlation coefficient (*r*) of 0.986 in a wide range, 4–20 radian s^{-1}. Thus, the image recognition method could be applied to the determination of the precise rotation rate with the same accuracy as the manual trajectory method.

The rotation rate was also evaluated for varying AC voltage (300 kHz). It is well known that the rotation rate depends on the square of the strength of the electric field from eq.2. The rotation rate increased linearly with the square of the applied voltage in the range of 0.8 Vpp to 2.4 Vpp (Fig. S9). When an AC voltage of less than 0.6 Vpp was applied, the cells did not rotate and drifted in place; when a voltage of 2.4 Vpp or more was applied, the cells rotated rapidly, making it difficult to analyze the rotation rate based on the image recognition method. In this study, cells were rotated at a relatively high rate by applying 2.0 Vpp to monitor the decrease in rotation rate associated with the shift in peak frequency caused by chemical stimulation.

We also evaluated the ROT behavior of K562 cells with different dielectric properties and slightly large diameters to Jurkat cells. The rotating electric fields with 300 kHz were applied after K562 cells were trapped in microwells (Fig. 5A). Almost K562 cells moved to the edges of the bottom electrodes without the rotation in microwells. However, K562 cells rotated at 11.8±0.46 radian s^{-1} (n=109 cells) by applying the frequency with 100 kHz (Fig. 5B). Real parts and imaginary parts of CM factor for K562 cells and Jurkat cells were calculated as a function of the frequency by using the values of their dielectric properties and diameter reported in previous work (Fig. 5C).[37] The value of the real part for K562 cells at 300 kHz was positive, while the value at 100 kHz was negative. Therefore, K562 cells experienced the attractive force of p-DEP at 300 kHz, resulting in the direction to the edges of electrodes. On the other hand, at 100 kHz, K562 cells were balanced at the center of microwells and would levitate from the bottom surface by the repulsive forces from 4 electrodes with the strong electric field (n-DEP), and were permitted to rotate at the center. Both parts for Jurkat cells shifted to higher frequency regions compared to those for K562 cells. Thus, no attractive force acted on Jurkat cells due to the negative value of Re[CM] below 300 kHz. These calculations significantly coincided with the experimental results for both cells (Fig. 3A and 5B). The rotation rate of Jurkat cells at 300 kHz (18.0±0.95 radian s^{-1} (n=48 cells)) was faster than that at 100 kHz (12.0±0.26 radian s^{-1} (n=113 cells)) (Fig. 5D) because it is in proportional to the value of Im[CM] (Eq. 2) that is maximum at approximately 300 kHz in the theoretical calculation (Fig. 5C). The results for Jurkat cells also coincided to the calculated Im[CM].

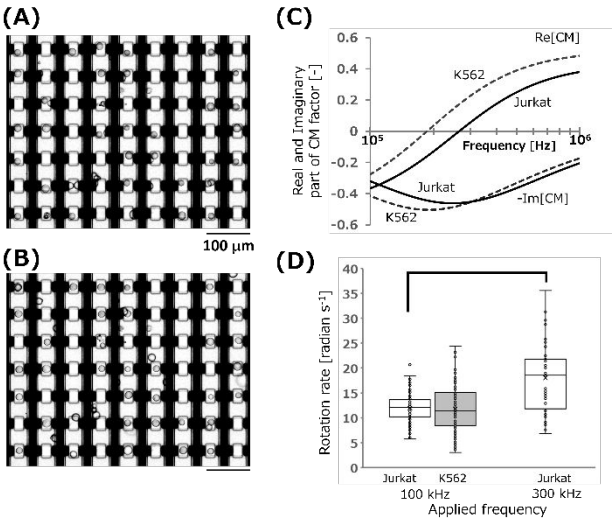

Rotation rate of the chemical stimulation-activated Jurkat cells

The microwell array device represents a superior platform for estimating the ROT responses of cells, following stimulation by chemical reagents in a real-time manner. To demonstrate the superiority of this electrode device, we monitored the ROT of

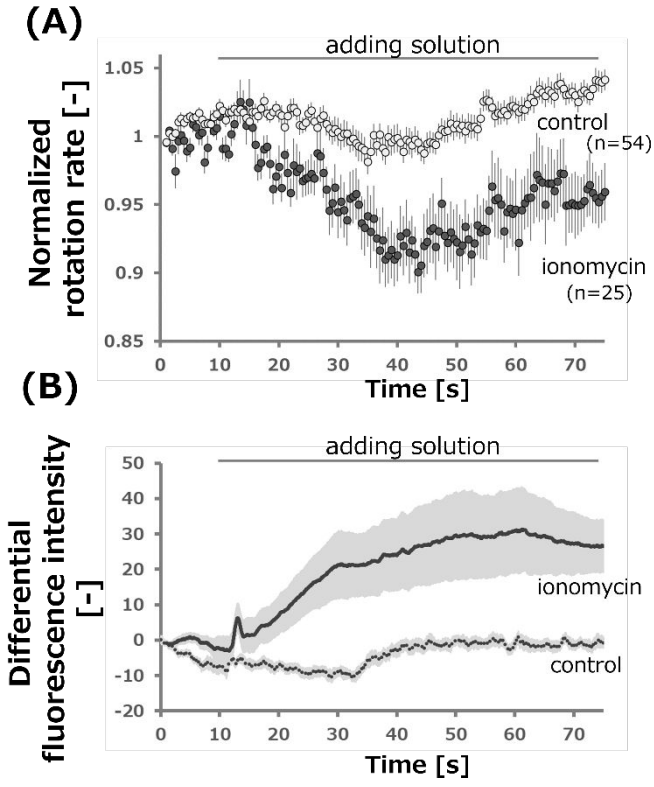

the Jurkat cells ionomycin (a calcium ionophore for inducing the expansions of the plasma membrane of cells) stimulation.[43,44] The ROT rates of Jurkat cells in continuous rotation at the same position were monitored before and after the addition of ionomycin-containing solution. Fig. 6 shows the rotation rates, following the addition of the ionomycin (1.0 μM)-containing ROT solution. The microwell-trapped cells began to rotate immediately when an AC voltage (300 kHz, 2.0 Vpp) was applied to the microband electrodes. The ROT solution containing ionomycin (1 μL) was gently added to the top of the suspension in the PDMS chamber (300 μL). When the solution was added, the cells on the insulating layer were resuspended by the convective flow. However, the cells trapped in the microwells were retained to rotate continuously. (see supporting Movies S3 and S4). The convective flow could not reach the bottom of the microwells because of the structure with the small opening of the microwells. The rotation rate decreased gradually for several seconds, following the addition of ionomycin at 10 s, reaching a peak at 40 s before returning to the original level. The time difference between the addition and response could be due to the diffusion of ionomycin in the microwell. The rotational rate was determined by the average of the normalized ROT rates of 25 cells. The normalized ROT rate was obtained by dividing the rotational rate at each time point by the average ROT rate in the first second. Figs. S10A and B show the images of five rotating cells, which were randomly selected, as extracted from Movie S3, and the typical time courses of the ROT rates obtained from them, respectively. The five cells were rotated continuously without any cell contamination in each microwell when recording the rotational motion. The range of the ROT rates of the five cells varied from 8.0 to 17.7 radian s^{-1}. However, their rotation rates were almost constant for the first 20 s even though the fluidic flow was caused by the addition of the ionomycin solution at 10 s. After the addition of the ionomycin solution (left end of Figure S10(A)), the cells that were drifting above the upper layer of the ROT device flowed from left to right in Fig. S10(A) (see supporting movie S3). The ROT rate of the cell (i), arranged at the leftmost in Fig. S10A, decreased earlier compared with those of the other four cells. This time difference in the onset of the decrease in the ROT rates might be due to the convectional flow of ionomycin from left to right in the image. Conversely, the depression of the average ROT rate of the cells that were stimulated by the solution without ionomycin was significantly low compared with that stimulated by the solution with ionomycin ($p = 0.0009$ at 40 s). Thus, the decrease in the rotation rate accounted for the effect of the added ionomycin, which would be detailed discussed.

We investigated the uptake of Ca^{2+} into the cytoplasm, following the addition of ionomycin. Figure 6B shows the fluorescence response of a Jurkat cell that was transfected with G-GECO, following the addition of the 1.0-μM ionomycin-containing ROT solution. The fluorescence intensity increased for several seconds after the addition of ionomycin and almost reached a plateau at 50 s. The result indicates that the concentration of Ca^{2+} in the cytoplasm increased with the

influx of extracellular Ca^{2+} supported by the added ionomycin. Notably, the response of the fluorescence intensity was very similar to that of the ROT rate. Thus, the decrease in the ROT rate might be due to the action of ionomycin on the cells. Finally, we also evaluated the change in the cell radius from the sequential images of the rotating cells (Fig. S11) since the CM factor depended on the cell radius and determined the ROT rate. Moreover, a significant influence of cell radius on the ROT rate has been reported.[20] Fig. S11 shows the time-course of the normalized cell radius. The cell radius was reduced by up to 2%, following the addition of the ionomycin-containing solution. This level of decrease was almost similar to that observed after adding solution without ionomycin; moreover, there was no significant difference between the cell radius with/without ionomycin at 40 s ($p = 0.14$ at 40 s). The slight change in the cell radius (Fig. S11) could be due to the misrecognition of the cell area during the extraction process of the cell contour caused by the displacement of the cell positions in the microwells and the shadow reflection of the cells flowing over the upper layer of the ROT device, following the addition of the solution. Therefore, the decrease in the rotation rate, following the addition of ionomycin, was very likely due to the interaction between ionomycin and the cell membrane rather than a decrease in the cell radius.

The extent of alteration in the membrane capacitance and conductance was evaluated from the decrease in the ROT rate in the presence of ionomycin. Recently, the large-scale plasma membrane expansion of Jurkat cells caused by the elevation of intracellular Ca^{2+} was reported by employing the patch-clamp measurement of the membrane capacitance and conductance.[43,44] This expansion approximately doubled the cell surface area and might result from the opening of the micro components on the plasma membrane rather than the expansion or reduction of the cell size. We calculated the **−**Im[CM] of the Jurkat cells when the AC voltage was applied at a frequency of 300 kHz at various membrane capacitances and conductance (Fig. S12). The value of −Im[CM] increased with the increasing membrane capacitance, peaking at 7.86 mF m^{-2} in the membrane capacitance and subsequently decreasing. Since the membrane capacitance of the Jurkat cells was assumed to be 9.82 mF m^{-2} in this study, the obtained value of −Im[CM] was −0.45, as indicated by the black circle in Fig. S12A. The addition of ionomycin reduced the ROT rate by up to 10% (Fig. 6A) compared with before its addition. Eq. (2) shows that the ROT rate was proportional to −Im[CM], indicating that −Im[CM] decreased by 10% assuming that the other parameters expressed in Eq. (2) remained constant during the ROT measurement. Thus, we observed that the membrane capacitance increased to 13.7 mF m^{-2}, which corresponded to a 40% increase (Fig. S12A). This increase in the membrane capacitance was slightly lower than the previously reported increase with the addition of 5 μM ionomycin in the solution containing 2 mM Ca^{2+}.[43] This difference might be due to the utilization of an ROT solution with a low Ca^{2+} concentration (2.1 μM) as the extracellular solution. We also evaluated the effect of the membrane conductance on the value of -Im [CM] (see appendix and Fig S12B). It has been reported that the addition of ionomycin led to a transient increase of membrane conductance from zero to approximately 60 nS.[43,44] The values of -Im [CM] at 300 kHz were calculated with various membrane conductance and found to be almost constant until 160 nS (Fig S12B). From these calculations, we conclude that the decrease of the rotation rate is due primarily to the increase in the membrane capacitance.

Discussion

In this study, we proposed a novel electrode device consisted with 225 microwells having four microelectrodes around the single microwells for simultaneously induce electrorotation to the vast number of cells. However, the ROT rates at various frequencies were required to accurately determine the dielectric properties of the membrane via the ROT method. Unfortunately, the current configuration of the ROT device complicates the initiation of ROT in the low-frequency (<100 kHz) and high-frequency (>1 MHz) regions because of the ejection of the cells from the microwells via n-DEP when an AC voltage is applied in the low-frequency region, as well as the attraction of the cells to the edge of the microelectrode via p-DEP when the AC voltage is applied in the high-frequency region. Although the frequency range is narrower, the simultaneous acquisition of many ROT rates around the crossover frequency in which the net force in DEP is zero, would improve the accuracy of estimating the membrane capacitance that was obtained by fitting to the theoretical ROT rate, which was calculated from Eq. (2).

Conclusions

We developed a novel device for simultaneous real-time ROT measurements, following stimulation with a chemical reagent via a fluidic flow, as well as an algorithm based on image recognition. The device, which comprised 225 microwells, induced ROT in approximately 70 cells in a single operation. The ROT rates of these single cells were evaluated via image recognition. In this study, the ROT rate was employed to monitor the expansion in the plasma membrane of Jurkat cells, following ionomycin stimulation. The ROT rate of the Jurkat cells was 10% lower than the initial rate (30 s) after the addition of ionomycin. The time-course of the decrease in the ROT rate was significantly similar to the increase in the intracellular calcium ion concentration owing to the effect of ionomycin. The decrease in the ROT rate reflected the increase in the membrane capacitance owing to the increase in the membrane area induced by the opening up of the micro components on the plasma membrane. We believe that this device represents a unique platform for the easy acquisition of membrane capacitance although the accuracy of the obtained dielectric properties can be improved.

Author Contributions

S. K. and M.S. performed the experiments. S. K. and M. S. analyzed the experimental data. S.C.-F. and S. U. developed the software for estimating the ROT rates. R.Y. and M.S. simulated the electric field. M. S. and T. Y. conceived the project. S. K., M. S., and T. Y. drafted the manuscript.

Conflicts of Interest

There are no conflicts to declare.

Acknowledgments

This work was supported by JKA and its promotion funds from AUTORACE to MS, A-STEP from JST Grant Number JPMJTM20QR to MS, SCORE-GAP fund from JST to MS, and JSPS KAKENHI Grant Numbers 19K05548 to MS and 20H02771 to TY, Grant-in-Aid for Scientific Research on Innovative Areas Platforms for Advanced Technologies and Research Resources "Advanced Bioimaging Support."

Notes and References

1 T. Tang, Y. Hosokawa, T. Hayakawa, Y. Tanaka, W. Li, M. Li and Y. Yalikun, *Engineering*, 2022, **10**, 110–126.
2 M. Xie, *The International Journal of Advanced Manufacturing Technology*, 2019, **105**, 4953–4966.
3 A. Banerjee, S. Chowdhury and S. K. Gupta, *IEEE Robot Autom Mag*, 2014, **21**, 81–88.
4 A. Shakoor, W. Gao, L. Zhao, Z. Jiang and D. Sun, *Microsyst Nanoeng*, 2022, **8**, 47.
5 B. Lim, V. Reddy, X. Hu, K. Kim, M. Jadhav, R. Abedini-Nassab, Y.-W. Noh, Y. T. Lim, B. B. Yellen and C. Kim, *Nat Commun*, 2014, **5**, 3846.
6 C. P. Moerland, L. J. van IJzendoorn and M. W. J. Prins, *Lab Chip*, 2019, **19**, 919–933.
7 F. Berndt, G. Shah, R. M. Power, J. Brugués and J. Huisken, *Nat Commun*, 2018, **9**, 5025.
8 D. Ahmed, A. Ozcelik, N. Bojanala, N. Nama, A. Upadhyay, Y. Chen, W. Hanna-Rose and T. J. Huang, *Nat Commun*, 2016, **7**, 11085.
9 S. Mohanty, I. S. M. Khalil and S. Misra, *Proceedings of the Royal Society A: Mathematical, Physical and Engineering Sciences*, 2020, **476**, 20200621.
10 Q. Tang, F. Liang, L. Huang, P. Zhao and W. Wang, *Biomed Microdevices*, 2020, **22**, 13.
11 J. Zhu, Q. Zhang, F. Liang, Y. Feng and W. Wang, *Journal of Micromechanics and Microengineering*, 2021, **31**, 124004.
12 N. F. Läubli, M. S. Gerlt, A. Wüthrich, R. T. M. Lewis, N. Shamsudhin, U. Kutay, D. Ahmed, J. Dual and B. J. Nelson, *Anal Chem*, 2021, **93**, 9760–9770.
13 C. Chen, Y. Gu, J. Philippe, P. Zhang, H. Bachman, J. Zhang, J. Mai, J. Rufo, J. F. Rawls, E. E. Davis, N. Katsanis and T. J. Huang, *Nat Commun*, 2021, **12**, 1118.
14 M. Mansor and M. Ahmad, *Int J Mol Sci*, 2015, **16**, 12686–12712.
15 W. M. Arnold and U. Zimmermann, *Zeitschrift fur Naturforschung - Section C Journal of Biosciences*, 1982, **37**, 908–915.
16 J. Yang, Y. Huang, X.-B. B. X. Wang, X.-B. B. X. Wang, F. F. Becker and P. R. C. Gascoyne, *Biophys J*, 1999, **76**, 3307–3314.
17 Y. Huang, X.-B. Wang, P. R. C. Gascoyne and F. F. Becker, *Biochimica et Biophysica Acta (BBA) - Biomembranes*, 1999, **1417**, 51–62.
18 M. Kiesel, R. Reuss, J. Endter, D. Zimmermann, H. Zimmermann, R. Shirakashi, E. Bamberg, U. Zimmermann and V. L. Sukhorukov, *Biophys J*, 2006, **90**, 4720–4729.
19 V. L. Sukhorukov, D. Imes, M. W. Woellhaf, J. Andronic, M. Kiesel, R. Shirakashi, U. Zimmermann and H. Zimmermann, *Biochimica et Biophysica Acta (BBA) - Biomembranes*, 2009, **1788**, 1841–1850.
20 A. W. Griffith and J. M. Cooper, *Anal Chem*, 1998, **70**, 2607–2612.
21 R. Takeuchi, M. Suzuki and T. Yasukawa, *Analytical Sciences*, 2021, **37**, 229–232.
22 X.-B. Wang, Y. Huang, P. R. C. Gascoyne, F. F. Becker, R. Hölzel and R. Pethig, *Biochimica et Biophysica Acta (BBA) - Biomembranes*, 1994, **1193**, 330–344.
23 G. Bahrieh, M. Erdem, E. Özgür, U. Gündüz and H. Külah, *RSC Adv.*, 2014, **4**, 44879–44887.
24 L. Huang, P. Zhao and W. Wang, *Lab Chip*, 2018, **18**, 2359–2368.
25 P. Benhal, J. G. Chase, P. Gaynor, B. Oback and W. Wang, *Lab Chip*, 2014, **14**, 2717–2727.
26 L. Huang, F. Liang, Y. Feng, P. Zhao and W. Wang, *Microsyst Nanoeng*, 2020, **6**, 57.
27 C. Reichle, T. Schnelle, T. Müller, T. Leya and G. Fuhr, *Biochimica et Biophysica Acta (BBA) - Bioenergetics*, 2000, **1459**, 218–229.
28 L. Huang, L. Tu, X. Zeng, L. Mi, X. Li and W. Wang, *Micromachines (Basel)*, 2016, **7**, 141.
29 C. Reichle, T. Müller, T. Schnelle and G. Fuhr, *J Phys D Appl Phys*, 1999, **32**, 2128–2135.
30 S.-I. Han, Y.-D. Joo and K.-H. Han, *Analyst*, 2013, **138**, 1529.
31 P. Benhal, G. Chase, P. Gaynor, B. Oback and W. Wang, *Int J Adv Robot Syst*, 2015, **12**, 84.
32 Y. C. Kung, K. W. Huang, W. Chong and P. Y. Chiou, *Small*, 2016, **12**, 4302.
33 Y. C. Kung, T. Man, K. W. Huang, W. Chong, J. King and P. Y. Chiou, in *2017 IEEE 12th International Conference on Nano/Micro Engineered and Molecular Systems, NEMS 2017*, Institute of Electrical and Electronics Engineers Inc., 2017, pp. 355–359.
34 M. Eguchi, K. Horio, F. Kuroki, H. Imasato and T. Yamakawa, in *World Automation Congress Proceedings*, IEEE Computer Society, 2018, vol. 2018-June, pp. 136–139.
35 K. Keim, M. Z. Rashed, S. C. Kilchenmann, A. Delattre, A. F. Gonçalves, P. Éry and C. Guiducci, *Electrophoresis*, 2019, **40**, 1830–1838.
36 K. Ino, A. Ishida, K. Y. Inoue, M. Suzuki, M. Koide, T. Yasukawa, H. Shiku and T. Matsue, *Sens Actuators B Chem*, 2011, **153**, 468–473.
37 S. Kawai, M. Suzuki, S. Arimoto, T. Korenaga and T. Yasukawa, *Analyst*, 2020, **145**, 4188–4195.
38 Y. Zhao, S. Araki, J. Wu, T. Teramoto, Y. F. Chang, M. Nakano, A. S. Abdelfattah, M. Fujiwara, T. Ishihara, T. Nagai and R. E. Campbell, *Science (1979)*, 2011, **333**, 1888–1891.
39 N. Otsu, *IEEE Trans Syst Man Cybern*, 1979, **SMC-9**, 62–66.
40 R. Pethig, *Dielectrophoresis*, John Wiley & Sons, Ltd, Chichester, UK, 2017.
41 Hywel Morgan and Nicolas G Green, *AC Electrokinetics: colloids and nanoparticles*, Research Studies Press Ltd, England, 2003.
42 J. Cottet, O. Fabregue, C. Berger, F. Buret, P. Renaud and M. Frénéa-Robin, *Biophys J*, 2019, **116**, 12–18.
43 C. Bricogne, M. Fine, P. M. Pereira, J. Sung, M. Tijani, Y. Wang, R. Henriques, M. K. Collins and D. W. Hilgemann, *Sci Rep*, 2019, **9**, 619.

44 C. Deisl, D. W. Hilgemann, R. Syeda and M. Fine, *Nat Commun*, 2021, **12**, 4990.

Figure Legends

Figure 1. (A) Micrograph and (B) cross-sectional view of the microwell array device. The inset in (A) is a magnified view of a single microwell. The cross-sectional views are (i)–(ii) and (iii)–(iv) of the magnified photographs

Figure 2. Ratio of the number of Jurkat cells trapped in a single microwell at various (A) incubation times and (B) cell concentrations injected into the PDMS chamber. (C) Microscopic images of Jurkat cells on microwells at various cell concentrations.

Figure 3. (A) Microscopic image of the rotating Jurkat cells in the microwell array device, following the application of an AC voltage of 300 kHz frequency and 2 Vpp voltage. Bar scale is 100 μm. (B) Sequential images of a single Jurkat cell rotating in the dashed white circle (i) in (A). Black arrow represents the characteristic point of this cell. (C) Heatmap of the NCC values of the cell in (B) analyzed via the image recognition method. (D) Time-course of the rotation rate of the single Jurkat cell in (B). Acquired value means the rotation rate obtained by substituting the number of frames from frame N to the frame with the first maximum NCC value into eq. (1). Moving average means the rotation rate obtained by averaging 30 consecutive acquired values (corresponding to 1 s).

Figure 4. Linear correlation between the rotation rates obtained by image recognition and visual analysis. The cells were subjected to ROT on the microwell array device by applying AC voltage (300 kHz and 2 Vpp)

Figure 5. Microscopic images of K562 cells on the ROT device when applying AC voltage with (A) 300 kHz and (B) 100 kHz. (C) Plots of the Re[CM] and –Im[CM] for Jurkat cell and K562 cell at various frequencies. (D) Rotation rates for Jurkat cells and K562 cells when applying AC voltages with 100 kHz and 300 kHz.

Figure 6. (A) Time-series of the normalized ROT rate (ratio to the ROT rate in the first seconds). One microliter droplet of the ROT solution without (white circle) or with (black circle) ionomycin was added at t = 10 s. (B) Time-series of the differential fluorescent intensity of the Jurkat cells that were transfected with G-GECO1.2. One microliter droplet of the ROT solution containing ionomycin that was added at t = 10 s

Keywords: Electrorotation, Single-cell analysis, Membrane capacitance, Calcium imaging, Dielectrophoresis